12th International Symposium on Turbulence and Shear Flow Phenomena (TSFP12)
Osaka, Japan, July 19–22, 2022

THE EFFECT OF SWEEP-ANGLE VARIATION ON THE TURBULENCE STRUCTURE IN HIGH SPEED TURBULENT REACTIVE FLOWS

Radouan Boukharfane
Mohammed VI Polytechnic University
MSDA group, Benguerir, Morocco
radouan.boukharfane@um6p.ma

Safae El Misaoui
Mohammed VI Polytechnic University
MSDA group, Benguerir, Morocco
safae.elmisaoui@um6p.ma

Matteo Parsani
King Abdullah University of Science and Technology
CEMSE, ECRC, Thuwal, KSA
matteo.parsani@kaust.edu.sa

Nilanjan Chakraborty
School of Engineering, Newcastle University
Newcastle-Upon-Tyne, United Kingdom
nilanjan.chakraborty@newcastle.ac.uk

ABSTRACT

The relevance of quantifying heat release and compressibility effects in turbulent compressible spatially developing shear flows using detailed kinetics as well as detailed multicomponent transport description is of important relevance in the operation of supersonic air-breathing engines, whose efficiency closely depends on the molecular mixing between oxidizer and fuel. The present study is devoted to investigated how the variation of a single parameter applied at the inlet, namely the sweeping (or skewness) angle, affects the turbulence structure and the evolution of the flow in a compressible and multi-component inert and reacting mixing layers using detailed chemistry and multicomponent transport. The preliminary computations indicate that the transitional region and the fully developed turbulence region depends strongly on the degree of flow sweeping at the inlet. The qualitative inspection of the results indicates the sweeping angle tends to increase more quickly the growth of the inlet structures, leading therefore to an enhancement the development of the mixing region. This is confirmed with the time-averaged statistics that characterize the mixing layer development. One possible perspective of the present work concerns flow control of mixing layer setup and reliable comparison between experiment, simulations and turbulence modelling.

INTRODUCTION

A significant amount of research has been done studying various aspects of reactive compressible turbulent shear flows in which the two mixing layers emerged between the injected fuel and the surrounding supersonic airflow within the combustion chamber are assumed to be parallel. However, sweeping effects due to controllable or uncontrollable lack of perfect alignment in practical applications or even experiments, which can affect the development of turbulence, have been addressed much more rarely, even though the the concept of enhancing mixing through the introduction of a swirl effect is quite old. Swithebank & Chigier (1969) considered several skew angles and concluded that the sweeping effect is responsible for increased mixing in the incompressible turbulent round jet flow and might cause similar results in compressible flows as well. Kaltenbach (2003) performed a series of direct numerical simulation (DNS) of flow over a swept rearward-facing step and explored the changes in the statistical turbulence structure due to a variation of a sweep angle from to 0° up to 60°. More recently, Meldi *et al.* (2020) carried out a parametric variations applied both on the sweeping angles and the shear intensity parameter applied at the inlet of an incompressible mixing layer. Despite previous interest in supersonic combustion, few compressible reacting shear flows have been investigated recently. On the one hand, a few experiments based on a configuration close to a mixing layer with convective Mach numbers below 0.4 have been conducted (Cheng *et al.*, 1994). On the other hand, few compressible reacting shear flows have been investigated recently To address the above issues in the flow transition and self-similarity regions and address some of the inconsistent conclusions in comparison with experiments about the Reynolds stress tensor evolution in the self-similar region, a comprehensive DNS study of a compressible mixing layer at $\mathrm{Ma}_c = 0.48$ is conducted with the objective to extend the previous works of Boukharfane *et al.* (2021*a*) and Boukharfane *et al.* (2021*b*) by assessing the relative impact of the inlet skew angle on the turbulence structure and the flow evolution while considering heat release effects, multicomponent mixtures and detailed transport models.

1 NUMERICAL SOLVER

The unsteady, three-dimensional, compressible Navier-Stokes equations are considered for a multi-species reactive gas mixture:

$$\begin{cases} \partial_t \rho + \partial_j \left(\rho \mathrm{u}_j \right) = 0, & \text{(1a)} \\ \partial_t \left(\rho \mathrm{u}_i \right) + \partial_j \left(\rho \mathrm{u}_i \mathrm{u}_j \right) + \partial_i \mathfrak{p} = \partial_j \tau_{ij}, & \text{(1b)} \\ \partial_t \left(\rho \mathfrak{e}_t \right) + \partial_j \left(\rho \mathfrak{e}_t + \mathfrak{p} \right) \mathrm{u}_i = \partial_j \left(\mathrm{u}_i \tau_{ij} \right) - \partial_j \mathfrak{q}_j, & \text{(1c)} \\ \partial_t \left(\rho \mathscr{Y}_\alpha \right) + \partial_j \left(\rho \mathrm{u}_j \mathscr{Y}_\alpha \right) = -\partial_j \left(\rho \mathscr{Y}_\alpha \mathrm{u}_{\alpha j} \right) + \rho \dot{\omega}_\alpha. & \text{(1d)} \end{cases}$$

where

$$\begin{cases} \mathfrak{q}_j = -\lambda \partial_j \mathscr{T} + \sum_{\alpha=1}^{\mathscr{N}_{\mathrm{sp}}} \rho \mathscr{Y}_\alpha \mathrm{u}_{\alpha j} \left(\mathfrak{h}_\alpha + \mathscr{R} \mathscr{T} \widetilde{\chi}_\alpha / \mathscr{W}_\alpha \right), \\ \rho Y_\alpha \mathrm{u}_{\alpha i} = -\sum_{\beta=1}^{\mathscr{N}_{\mathrm{sp}}} \rho \widetilde{\mathscr{D}}_{\alpha\beta} \left(\partial_j X_\beta + \frac{X_\beta - \mathscr{Y}_\beta}{\mathfrak{p}} \partial_j \mathfrak{p} \right) \end{cases}$$

and

$$\dot{\omega}_\alpha = \sum_{i=1}^{\mathscr{N}_{\rm re}} \left(\nu''_{\alpha,i} - \nu'_{\alpha,i}\right) \left(\mathtt{k}_i^f \prod_{\alpha=1}^{\mathscr{N}_{\rm sp}} [X_\alpha]^{\nu'_{\alpha,i}} - \mathtt{k}_i^r \prod_{\alpha=1}^{\mathscr{N}_{\rm sp}} [X_\alpha]^{\nu''_{\alpha,i}} \right),$$

This system of conservative equations is based on the following set of variables. The letter t represents the time and the symbols ∂_t and ∂_i denote the partial differential operators ∂/∂_t and $\partial/\partial x_i$, respectively. The velocity component in direction i is denoted by u_i, the density by ρ, the pressure by $\mathfrak{p}$, the total energy (the sum of the internal specific energy, $\mathfrak{e}$, and the kinetic energy) by $\mathfrak{e}_t = \mathfrak{e} + \mathrm{u}_i\mathrm{u}_i/2$, and the mass fraction of the $\alpha^{\rm th}$ species by $\mathscr{Y}_\alpha$ (with $\alpha = 1, \cdots, \mathscr{N}_{\rm sp}$, where the integer $\mathscr{N}_{\rm sp}$ denotes the number of species). Herein, the density, pressure, and temperature, $\mathscr{T}$, are interrelated through the ideal gas law, $\mathfrak{p} = \rho\mathscr{R}\mathscr{T}/\mathscr{W}$, where $\mathscr{W}^{-1} = \sum_{\alpha=1}^{N} \mathscr{Y}_\alpha/\mathscr{W}_\alpha$ and $\mathscr{W}_\alpha$ is the molecular mass of of the $\alpha^{\rm th}$ species. The stress tensor is evaluated as $\tau_{ij} = \mu\left(\partial_j \mathrm{u}_i + \partial_i \mathrm{u}_j\right) + \left(\kappa - 2\mu/3\right)\partial_k \mathrm{u}_k \delta_{ij}$, where μ refers to the dynamic viscosity and κ to the bulk viscosity. λ stands for the thermal conductivity and $\mathfrak{h}_\alpha$ for the sensible enthalpy of the chemical specie α. $\nu''_{\alpha,i}$ and $\mathtt{k}_i^f$ stand, respectively, the forward stoichiometric coefficient and the forward rate constant of the i-elementary reaction ($\mathscr{N}_{\rm re}$ being the number of reactions), whereas $\nu'_{\alpha,i}$ and $\mathtt{k}_i^r$ are their reverse counterparts. The rate constants are assumed to obey an Arrhenius law and $[X_\alpha]$ are the molar concentrations of species α.

The viscous and molecular diffusion flux functions are computed using an eighth-order centred finite difference scheme. The temporal integration is performed by using a third-order total variation diminishing (TVD) Runge–Kutta algorithm (Gottlieb & Shu, 1998). The enthalpies and specific heat capacities at constant pressure of each species are expressed as polynomial forms of temperature using a series of coefficients determined from the JANAF databases (Prophet *et al.*, 1971). A detailed verification of the solver may be found in Boukharfane (2018), which assembles five elementary and verification subsets including the Sod's shock tube problem, the ignition sequence of a multi-species mixture in a shock tube, a one-dimensional laminar premixed flame, isentropic vortex, and shock–vortex interactions.

2 SIMULATION SETUP

The turbulent spatially evolving mixing layers is a flow originating from the interaction between two homogeneous streams having different asymptotic, high $\mathbb{U}^h$ (or hot oxidizer stream $O_2/H_2O/N_2$) and low $\mathbb{U}^l$ (or cold fuel stream H_2/N_2) speed stream velocities. The sweeping of the spatially mixing layers indicate a lack of perfect alignment between the two parallel and asymptotic velocities by a constant angle ζ measured on the x_1–x_3 planes in such manner that $\mathbf{u}^h = \left(\mathbb{U}^h, 0, 0\right)$ and $\mathbf{u}^l = \left(\mathbb{U}^l \cos\zeta, 0, \mathbb{U}^l \sin\zeta\right)$. The flow at the inlet ($x_1 = 0$) is a hyperbolic tangent profile for the streamwise and spanwise velocities, species mass fractions and density/ All numerical simulations are initialized in the computational domain using the unperturbed hyperbolic tangent profile for the velocity, species mass fraction and density. The Reynolds number based on the initial vorticity thickness, the velocity difference $\Delta\mathbb{U} = \mathbb{U}^h - \mathbb{U}^l$, and the average dynamic viscosity is 640. Dirichlet boundary conditions are applied at the two supersonic inlets. Perfectly non–reflecting boundary conditions are set at the outflow and the cross–stream directions, whereas periodic boundary conditions are settled along the spanwise directions. For equal densities and specific heats, the effects of compressibility on the shear-layer growth rate is often identified through the convective Mach Number, $\mathrm{Ma}_c = \Delta\mathbb{U}/(\mathfrak{c}^h + \mathfrak{c}^l)$. For the present study, it is set to $\mathrm{Ma}_c = 0.48$. A schematic of the computational arrangement is shown in Fig. 1. The size of the computational domain for each case is set as $\left(\mathrm{L}_{x_1} \times \mathrm{L}_{x_2} \times \mathrm{L}_{x_3}\right)/\delta_\omega^0 = 520 \times 120 \times 60$ resolved by $\mathscr{N}_{x_1} \times \mathscr{N}_{x_2} \times \mathscr{N}_{x_3} = 2300 \times 400 \times 200$ grid points. In addition to the reference case, corresponding to $\zeta = 0°$, three numerical simulations of mixing layers are conducted corresponding to three angles of sweeping, $\zeta = 5°$, $10°$ and $15°$.

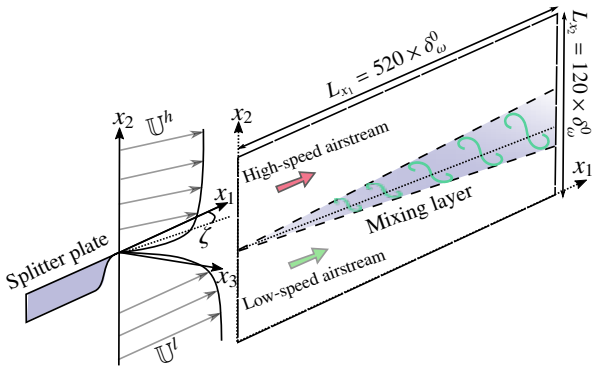

Figure 1: Schematic of the computational arrangement

2.1 NUMERICAL RESULTS

2.2 MIXING LAYER FLOW FIELD CHARACTERISTICS

The classical shapes and organization of the large-scale turbulent structures in the mixing layer is reported in fig. 6a and section 2.5. Compressibility effects are visible in the present setup due to absence of spanwise Brown-Roshko rollers and the presence of the three-dimensional and disorganized turbulent structures with a dominance of small-scale eddies. Heat release has also a noticeable impact in the transition of the mixing layers. Indeed, complex oblique flow structures grow and the formation of two-dimensional large structures is readily observed through the streamwise direction as a consequence of the relaminarizing effect induced by heat release; see fig. 6a and section 2.5. On the other hand, the sweeping mixing layers featuring a sweeping angle of $\zeta = 15°$ show a different flow pattern compared to the case $\zeta = 0$. In the first part of the mixing process, which features mainly two-dimensional spanwise vortices, the axis of the coherent structures in the case $\zeta = 15°$ is titled with respect to the normal incoming flow direction. In the unskewed case, the shear layers roll up into Λ-shaped vortices, which quickly evolve into hairpin vortices and then sheaths with intense vorticity and then break up into small slender vortices. The skewed case exhibits visibly no Λ-shaped vortices, only elongated sheaths are present near the inlet of the mixing layers that lately break up. In the second region characterized by the break-down of two-dimensional primary coherent structures to small-scale structures, the vortex roll-up process takes place early and the growth of inlet structures are more magnified in the presence of sweeping effects. Substantial increase of mixing-layer growth with the presence of skewness effects is observed. Moreover, the interactions between large-scale rollers and rib vortices that trigger the turbulence transition and the break down to small-scale structures occurs earlier with $\zeta = 15°$ compared to $\zeta = 0°$.

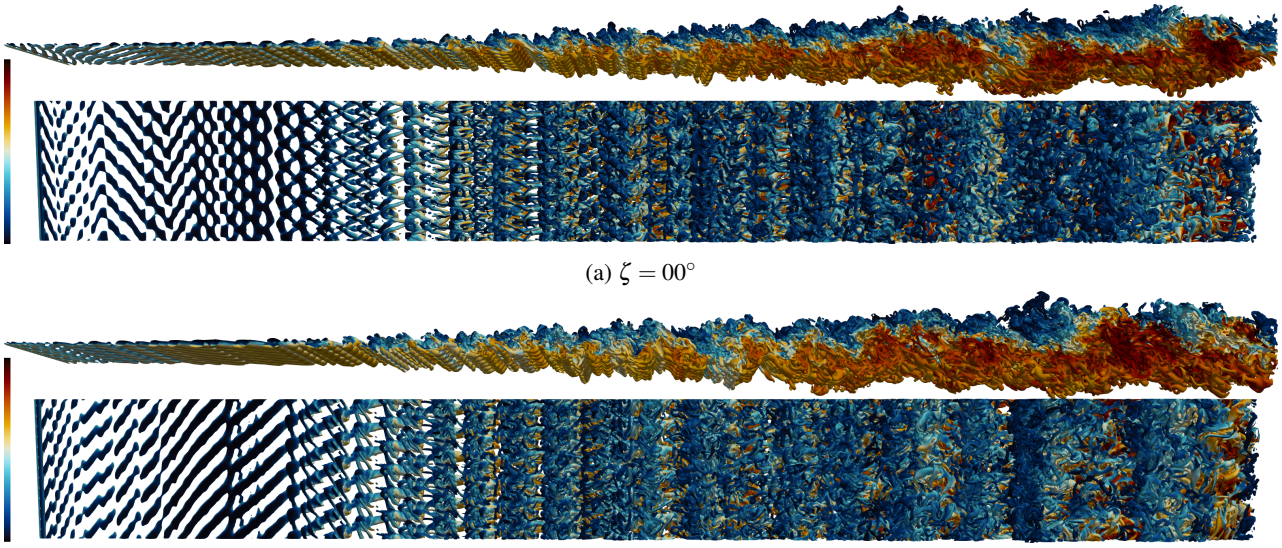

(a) $\zeta = 00°$

(b) $\zeta = 15°$

Figure 2: Q-criterion colored with local Mach number to visualize the development of coherent structures in the mixing layer for both angles of skewness.

2.3 GROWTH RATES

To have a rough estimation of the local size of the turbulent structures in the mixing layer, in Fig. 3 we show the momentum and vorticity thicknesses, normalized by $\eta\delta_\omega^0$, with $\eta = \|\mathbf{u}^h - \mathbf{u}^l\| / \|\mathbf{u}^h + \mathbf{u}^l\|$. Here, the momentum thickness is defined as follows

$$\delta_\theta = \frac{1}{\rho_0}\int_{-\infty}^{+\infty}\int_{-\infty}^{+\infty}\langle\rho\rangle\frac{\langle u_1\rangle_f - \mathbb{U}^h}{\|\mathbf{u}^h - \mathbf{u}^l\|}\left(1 - \frac{\langle u_1\rangle_f - \mathbb{U}^h}{\|\mathbf{u}^h - \mathbf{u}^l\|}\right)\mathrm{d}x_2\mathrm{d}x_3, \tag{2}$$

where ρ_0 stands for the arithmetic mean value between the densities of the oxidizer and fuel inlet streams $\rho_0 = (\rho^h + \rho^l)/2$. The mixing layer evolves to a self-similar state past $x_1/\delta_\omega^0 \approx 200$, regardless of the skew angle, whence near linear growth is observed. The vorticity thickness shows significant differences in the transition region, in which skewing promotes faster growth. Heat release has also a noticeable impact in the transition of the mixing layer since the reacting cases shows higher growth compared to the inert case as a consequence of the relaminarizing effect induced by heat release. The slopes of the vorticity thickness regression lines indicate small but consistent growth with the skew angle is observed also in the fully developed region, which is likely to be exploitable in Scramjet engines applications. The momentum thickness exhibits much less dependence on ζ, with exception of the the highest value under consideration, $\zeta = 15°$ and heat release tend to noticeably reduce the growth rate in the fully developed region of mixing layers.

2.4 REYNOLDS STRESSES

Further insight into the effects of flow skewing may be gained from inspection of distribution of the Reynolds stresses, which are also expected to reach an asymptotic self-similar regime. The streamwise and spanwise Reynolds stress profiles are shown as a function of the self-similar cross-stream coordinate x_2/δ_ω in Fig. 4. Both stresses exhibit tendency to collapse, and the streamwise stress profiles show moderate asymmetry, peaking in the region occupied by the heavier oxidizer (lower density region), as noted by Brown & Roshko (1974) and Pantano & Sarkar (2002). Although the unskewed

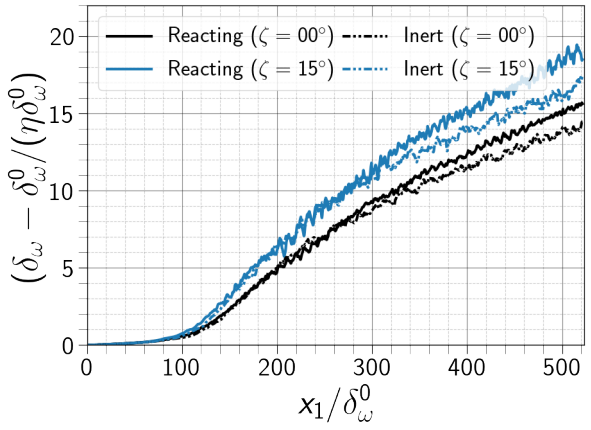

(a) $\zeta = 00°$

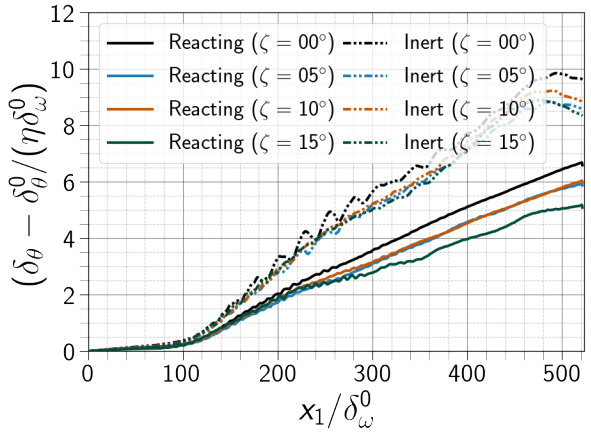

Figure 3: Comparison the streamwise evolution of (a) vorticity thickness and (b) momentum thickness of the mixing layer. The dashed lines denote fitted linear regression curve.

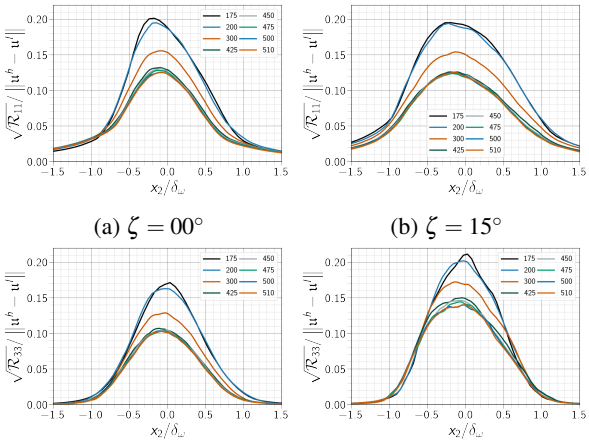

(a) $\zeta = 00°$ (b) $\zeta = 15°$

(c) $\zeta = 00°$ (d) $\zeta = 15°$

Figure 4: Profiles of streamwise (top row) and spanwise (bottom row) Reynolds stresses at various streamwise locations for $\zeta = 0°$ and $15°$. Solid lines corresponds to natural direction, while dashed lines stands for the mean convective direction.

case exhibits higher levels of the streamwise Reynolds stress in the development regime, skewed and unskewed cases achieve self-similarity at approximately the same streamwise location, $x_1/\delta^0_\omega = 450$, and the maximum level in the self-similar state is similar. The peak value of $\sqrt{\mathscr{R}_{11}}/\left\|u^h - u^l\right\|$ in the present simulation of 0.137 is close to the numerical data of Debisschop *et al.* (1994), who reported a value 0.141 at convective Mach number $\mathrm{Ma}_c = 0.525$. Stronger effect of skewing is found on the spanwise Reynolds stress $\sqrt{\mathscr{R}_{11}}/\left\|u^h - u^l\right\|$, for which the skewing yields substantially higher peak values both in the development and in the self-similar region. In the mean convection direction, $\sqrt{\mathscr{R}_{33}}/\left\|u^h - u^l\right\|$ exhibits naturally lower amplitude, whereas $\sqrt{\mathscr{R}_{11}}/\left\|u^h - u^l\right\|$ seems to be nearly independent of the system of coordinate in where it is computed.

The spatial evolution of the peak values of turbulent intensity distributions along the normalized streamwise x_1-direction is displayed in Fig. 5. The profile of peak intensities for both

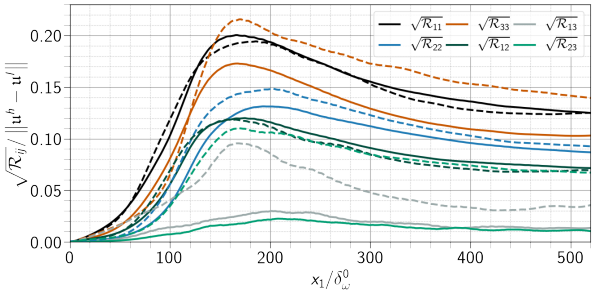

Figure 5: Peak values of turbulent intensity distributions along the normalized x_1-axis in (a) the natural direction and (b) in the mean convective direction. Solid lines: $\zeta = 00°$, and dashed lines: $\zeta = 15°$.

skewed and unskewed cases has a distribution different from the classical incompressible mixing layers, in which the peak intensities are achieved at almost the same normalized streamwise location for all the values of the components of Reynold stress, as in the present compressible mixing layers. The skewed case exhibits a peak values for streamwise turbulence intensity that start to rise upstream further compared to the unskewed case, but a lower peak value is reached. However, the streamwise intensity relaxes monotonically to an asymptotic value similar to the unskewed case, meaning that the peak value of $\mathscr{R}_{11}$ seems to be unaffected by skewing. However, the spanwise turbulent intensity experiences a sharp increase and decays to an asymptotic higher than $\mathscr{R}_{11}$. A possible explanation for these findings is that as the skew angle is increased, the elongation of large-scale turbulence structures become higher in the x_1-direction relative to x_2 and x_3 directions, which tends to be compensated further downstream by the increase of the fluctuations of $\mathscr{R}_{22}$ and, a mainly of $\mathscr{R}_{33}$. Beyond the maximum peaks, the turbulent intensities of $\mathscr{R}_{22}$ and $\mathscr{R}_{33}$ seem to be suppressed in the absence of skewing effect much faster, which indicates that skewed mixing layers induce more intense turbulence and enlarge the the momentum exchange between the turbulent structures and the inflow mainstream.In the mean convection direction, the components involving of spanwise direction x_3 present lower turbulent intensity peaks compared to the natural direction for the most skewed case.

2.5 ANISOTROPY EFFECT

A key tool in the development of advanced turbulence closures is the consideration of the anisotropy effects (Vreman *et al.*, 1996), which can be reformulated using either the Reynolds stress anisotropy

$$\mathfrak{b}^{\mathscr{K}}_{ij} = \frac{\mathscr{R}_{ij} - \frac{2}{3}\delta_{ij}\mathscr{K}}{2\mathscr{K}}, \tag{3}$$

or the dissipation anisotropy as

$$\mathfrak{b}^{\varepsilon}_{ij} = \frac{\varepsilon_{ij} - \frac{2}{3}\delta_{ij}\varepsilon}{2\varepsilon}, \tag{4}$$

where δ_{ij} is the Kronecker delta. The streamwise evolution of anisotropy tensor, where $\mathscr{R}_{ij}$ and $\mathscr{K}$ are integrated along the spatial mixing layer are displayed in Fig. 6 for $\zeta = 00°$ and $\zeta = 15°$. The similarity between $\mathfrak{b}^{\mathscr{K}}$ and $\mathfrak{b}^{\varepsilon}$ (not shown here) profiles indicates that the flow organization fairly influences the small scale turbulence structure, which induces almost the same anisotropy in both quantities. The other cases are not shown since the trends observed tends to amplify as ζ becomes bigger. The profiles of anisotropies is quite similar either using the Reynolds stress or dissipation tensors. In the pre-transitional regime, all the anisotropies increase to reach a peak value before converging to an almost asymptotic constant value in the self-similar region. Skewing the inlet inflow strongly affects the initial evolution of the anisotropies and alters their asymptotic values. As ζ increases, the $\mathfrak{b}^{\mathscr{K}}_{33}$ and $\mathfrak{b}^{\mathscr{K}}_{23}$ profile increase above zero, indicating that a higher level of skewing induces an increase of the level of anisotropy. The use of the isotropic assumptions will likely be inaccurate at higher skew angle ζ.

Given that the tensor $\mathfrak{b}^{\mathscr{K}}$ has zero trace, Lumley & Newman (1977) showed that all the anisotropy states are described by the two invariants of $\mathfrak{b}^{\mathscr{K}}$ given by

$$\mathbb{II}^{\mathscr{K}} = -\frac{1}{2}\left(\Lambda_1^2 + \Lambda_2^2 + \Lambda_3^2\right), \tag{5}$$

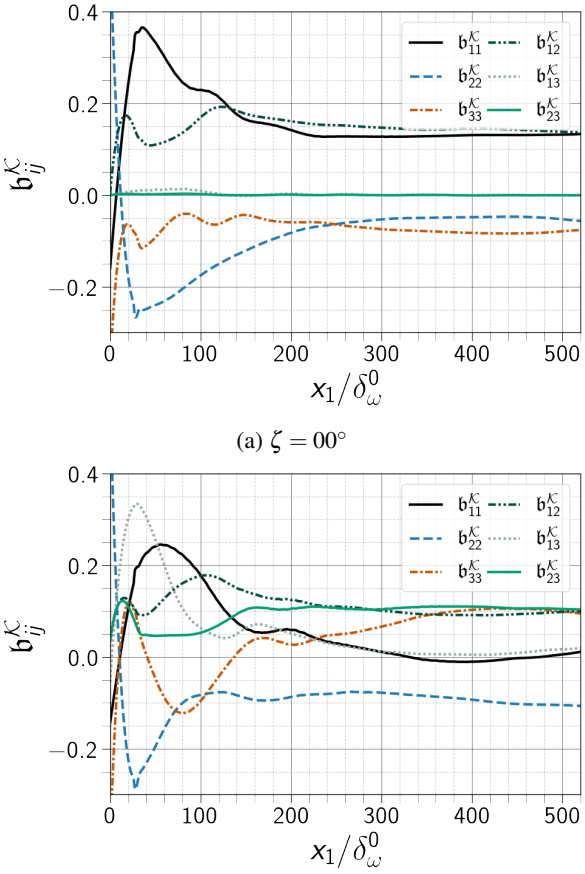

(a) $\zeta = 00°$

(b) $\zeta = 05°$

Figure 6: Longitudinal evolution of the anisotropy tensors $\mathfrak{b}^{\mathcal{K}}$.

and

$$\mathbb{III}^{\mathcal{K}} = \frac{1}{3}\left(\Lambda_1^3 + \Lambda_2^3 + \Lambda_3^3\right), \tag{6}$$

where Λ_1, Λ_2, and Λ_3 are the eigenvalues of $\mathfrak{b}^{\mathcal{K}}$. Physically, $\mathbb{II}^{\mathcal{K}}$ is an indicator of anisotropy in the flow, while $\mathbb{III}^{\mathcal{K}}$ denotes the nature of anisotropy. The different realizable anisotropic states of the turbulent velocity flowfield are contained within a triangle in the $\mathbb{II}^{\mathcal{K}}$-$\mathbb{III}^{\mathcal{K}}$ plan, the so-called Lumley triangle Lumley (1979). One should caution that the topology of of the energy distribution induced from the analysis of the $\mathbb{II}^{\mathcal{K}}$-$\mathbb{III}^{\mathcal{K}}$ plan should not be interpreted as the shape of the flow eddies since the characteristic shapes associated to the stresses and and those to the eddies are not generally equivalent (Simonsen & Krogstad, 2005). The resulting invariant mappings along the streamwise direction are portrayed in Fig. 7 for the skewing angles with the Lumley triangle boundaries labelled. The limiting states are shown by the three solid lines. In all the cases, the turbulence is essentially two-component in the transitional regime and three-component at the self-similarity state for all the case. The main difference occurs at the pre-transitional regime. Indeed, for the unskewed case and as the streamwise coordinate increases, the turbulence anisotropy is relatively approaching the axisymmetric expansion bound (rod-like shapes) and the isotropic state. However, as ζ becomes higher, the invariant mapping get closer to the one-component limit along the axisymmetric bound to the right. The flow slightly tends to be in close proximity to the plane-strain condition to the left-side of the Lumley triangle (axisymmetric disk-like state or oblate spheroid shape) as the skew angle becomes higher. These findings can also be observed by considering the determinant of the normalized Reynolds stress tensor $\mathbb{F}$, which is related to $\mathbb{II}^{\mathcal{K}}$ and $\mathbb{IIII}^{\mathcal{K}}$ as follows

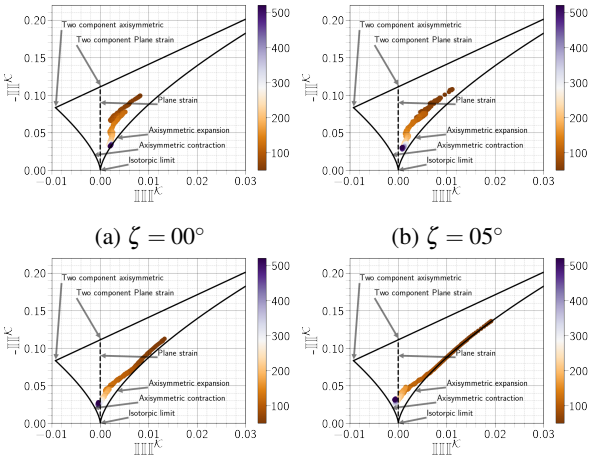

(a) $\zeta = 00°$

(b) $\zeta = 05°$

(c) $\zeta = 10°$

(d) $\zeta = 15°$

Figure 7: Reynolds stress anisotropy invariants using Lumley triangle constraints colored by the streamwise coordinate.

$$\mathbb{F} = 1 + 9\mathbb{III}^{\mathcal{K}} + 27\mathbb{IIII}^{\mathcal{K}}. \tag{7}$$

with $\mathbb{F}$ being one denote a perfectly isotropic and three-dimensional turbulence, and $\mathbb{F}$ being zero denote a pure two component turbulence and completely anisotropic. As shown in Fig. 8, all cases almost collapse on the self-similarity region (giving another statistical tool to measure self-similarity) and are close to unity, indicating an approach towards isotropy. None of the cases reach unity, meaning that the present flows exhibit anisotropy throughout the fields. The main effect of skewing occurs between the inlet of the computational domain and the transition to turbulence. In particular, the level is isotropy is lower as the skew angle becomes higher.

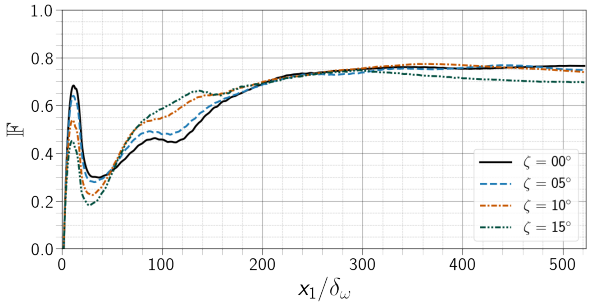

Figure 8: Longitudinal evolution of the invariant function $\mathbb{F}$.

3 CONCLUSION

In the present paper, structural evolution and turbulent statistics of a compressible mixing layer with $\mathrm{Ma}_c = 0.48$ are investigated employing direct numerical simulation to identify

the effect of skewness. Both instantaneous and time-averaged data are utilized to better understand the flow dynamical behaviors in the presence or not of skewness. The instantaneous visualization results indicate an amplification of the inlet disturbances resulting in a faster increase of the mixing process. The higher mixing layer growth rate is a direct consequence increaed velocity fluctuations, *i.e.*, increased turbulent kinetic energy and increased Reynolds stresses. Their increase with skewing effect is traced back to a decrease of the pressure-strain correlations and an increase of the production rate of the spanwise Reynolds stress. These correlations mainly steer the redistribution mechanism of turbulent fluctuating energy from the streamwise Reynolds stress component to the spanwise component. The peak streamwise normal stress showed little variation, while the transverse normal, spanwise normal, and primary shear stresses all increased in peak magnitude with increasing skew angle. In addition, Reynolds stress anisotropy observations were made. From the similarity profiles, the main effect of skewing were observed in the transition region. The invariant mappings of the mixing layers were found to tend toward the one component limit of the Lumley triangle as the skew angle is increased. A slightly reduction of all main terms in the Reynolds stress transport equations and the transport equation of the turbulent kinetic energy with increasing the skew angle ζ has been noticed, and an analysis of the corresponding transversely integrated terms has shown that the pressure-strain correlation of the streamwise Reynolds stress is directly connected to the momentum thickness growth rate and responsible for its increase.

REFERENCES

Boukharfane, R. 2018 Contribution à la simulation numérique d'écoulements turbulents compressibles canoniques. PhD thesis, École Nationale Supérieure de Mécanique et d'Aérotechnique.

Boukharfane, R., Er-raiy, A., Elkarii, M. & Parsani, M. 2021*a* A direct numerical simulation study of skewed three-dimensional spatially evolving compressible mixing layer. *Physics of Fluids* **33** (11), 115114.

Boukharfane, R., Er-Raiy, A., Parsani, M. & Hadri, B. 2021*b* Skewness effects on the turbulence structure in a high-speed compressible and multi-component inert mixing layers. In *AIAA Aviation 2021 Forum*, p. 2915.

Brown, G. L. & Roshko, A. 1974 On density effects and large structure in turbulent mixing layers. *Journal of Fluid Mechanics* **64** (4), 775–816.

Cheng, T. S., Wehrmeyer, J. A., Pitz, R. W., Jarrett Jr, O. & Northam, G. B. 1994 Raman measurement of mixing and finite-rate chemistry in a supersonic Hydrogen-air diffusion flame. *Combustion and Flame* **99** (1), 157–173.

Debisschop, J. R., Chambers, O. & Bonnet, J. P. 1994 Velocity field characteristics in supersonic mixing layers. *Experimental thermal and fluid science* **9** (2), 147–155.

Gottlieb, S. & Shu, C.-W. 1998 Total variation diminishing Runge–Kutta schemes. *Mathematics of Computation* **67** (221), 73–85.

Kaltenbach, H.-J. 2003 The effect of sweep-angle variation on the turbulence structure in a separated, three-dimensional flow. *Theoretical and Computational Fluid Dynamics* **16** (3), 187–210.

Lumley, J. L. 1979 Computational modeling of turbulent flows. In *Advances in Applied Mechanics*, , vol. 18, pp. 123–176. Elsevier.

Lumley, J. L. & Newman, G. R. 1977 The return to isotropy of homogeneous turbulence. *Journal of Fluid Mechanics* **82** (1), 161–178.

Meldi, M., Mariotti, A., Salvetti, M. V. & Sagaut, P. 2020 Numerical investigation of skewed spatially evolving mixing layers. *Journal of Fluid Mechanics* **897**.

Pantano, C. & Sarkar, S. 2002 A study of compressibility effects in the high-speed turbulent shear layer using direct simulation. *Journal of Fluid Mechanics* **451**, 329.

Prophet, H., Stull, D. R., United States & National Bureau of Standards 1971 *JANAF thermochemical tables*. U.S. Dept. of Commerce, National Bureau of Standards.

Simonsen, A. J. & Krogstad, P.-Å. 2005 Turbulent stress invariant analysis: Clarification of existing terminology. *Physics of Fluids* **17** (8), 088103.

Swithebank, J. & Chigier, N. A. 1969 Vortex mixing for supersonic combustion. In *Symposium (International) on Combustion*, , vol. 12, pp. 1153–1162. Elsevier.

Vreman, A. W., Sandham, N. D. & Luo, K. H. 1996 Compressible mixing layer growth rate and turbulence characteristics. *Journal of Fluid Mechanics* **320**, 235–258.